Materials Characterization 131 (2017) 39–48

Contents lists available at ScienceDirect

Materials Characterization

journal homepage: www.elsevier.com/locate/matchar

Characterization of the inner structure of porous TiO_2 nanoparticle films in dye sensitive solar cells (DSSC) by focused ion beam (FIB) tomography and transmission Kikuchi diffraction (TKD) in the scanning electron microscope (SEM)

Nicole Wollschläger[a,*], Laurie Palasse[b], Ines Häusler[a], Kai Dirscherl[d], Frédéric Oswald[c], Stéphanie Narbey[c], Erik Ortel[a], Vasile-Dan Hodoroaba[a,*]

[a] Bundesanstalt für Materialforschung und -prüfung (BAM), Unter den Eichen 87, D-12205 Berlin, Germany
[b] Bruker Nano GmbH, Am Studio 2, D-12489 Berlin, Germany
[c] Solaronix SA, Rue de l'Ouriette 129, CH-1170 Aubonne, Switzerland
[d] Danish Fundamental Metrology, Matematiktorvet 307, 2800 Kongens Lyngby, Denmark

ARTICLE INFO

Keywords:
Transmission Kikuchi diffraction
Focused ion beam tomography
Titanium dioxide nanoparticles
Porosity
Particle size
DSSC

ABSTRACT

A combined methodical approach is tested for the first time with respect to the characterization of the inner structure of porous TiO_2 layers infiltrated with ruthenium molecular sensitizer as typically used in modern dye sensitized solar cells (DSSC). Their performance is directly linked to the surface area 'offered' by the pore network to the dye. The micrometer thick layer employed was manufactured by screen-printing of a starting TiO_2 powder constituted of shape-controlled, bipyramidal anatase nanoparticles (NPs) on FTO/glass substrates. The analytical methods exploited in our study are Focused Ion Beam (FIB) slicing followed by 3D reconstruction as well as the new approach transmission Kikuchi diffraction (TKD) technology in the scanning electron microscope (SEM). While the first method results in the visualization of the 3D pore network within the TiO_2 layer, the second one can be successfully applied to analyze the crystal orientation of grains (i.e. NPs in our case) in nanometer resolution. Moreover, size and shape distribution of the TiO_2 NPs within the layer can be extracted. SEM in transmission mode and atomic force microscopy (AFM) have been used to verify the dimensional data obtained by the new combined methodical approach. Its analytical benefits but also the challenges and limitations are highlighted.

1. Introduction

Dye sensitized solar cells (DSSCs) attracted great attention to the scientific community as a potentially efficient conversion system, also compared to other photovoltaic energy conversion systems. The core of a DSSC consists of a film, such as titanium dioxide, as charge carrier on a transparent glass substrate. The titania film is coated with a light-sensitive compound. In accordance with the idea of Grätzel and O'Reagan, a redox pair (usually iodide/triiodide) provides holes after the photoelectrical reaction to close the redox cycle [1].

The conversion efficiency of the firstly developed DSSCs reached about 7%. In consequence, lot of effort has been invested to optimize certain parts of the DSSC system [2,3]. For instance, a series of sensitizer molecules with ruthenium as a core element were synthesized to enhance stability and adsorption range in the near infra-red (IR) spectral region. Consequently, the efficiency of DSSCs could be improved to 14% [4]. The sensitizer is directly bonded to a titanium dioxide layer representing the charge carrier of the system; its nature determines the amount of adsorbed sensitizer as well as the quality of electron transport. Besides compact films, porous layers consisting of single crystalline titania nanoparticles (NPs) were also tested [5–9]. Preparation of such nanoparticle layers is simple, also at industrial scale, via screen-printing techniques. Layers provide by the inner porous layer structure a large surface area for sensitizer attachment, but also grain boundaries, which reduce the internal light reflection. Further improvements must be well balanced out, the quality of such nano-particulate layers in terms of their inner structure must be checked routinely. Herein, both the investigation of the assembled particles as individual entities and

* Corresponding authors.
E-mail addresses: Nicole.Wollschlaeger@bam.de (N. Wollschläger), Laurie.Palasse@bruker.com (L. Palasse), Ines.Haeusler@bam.de (I. Häusler), kdi@dfm.dk (K. Dirscherl), frederic.oswald@solaronix.com (F. Oswald), stephanie.narbey@solaronix.com (S. Narbey), Dan.Hodoroaba@bam.de (V.-D. Hodoroaba).

http://dx.doi.org/10.1016/j.matchar.2017.06.030
Received 26 April 2017; Received in revised form 27 June 2017; Accepted 28 June 2017
Available online 29 June 2017
1044-5803/

the characteristics of the nano-particulate layer as a whole are of great interest to clarify the relation between particles size, particles shape, film porosity and the resulting efficiency of the cell. Especially homogeneously distributed particles and pores were found to enhance the overall cell efficiency [10].

The accurate characterization of NPs as powder or in suspended form is per se a challenging task; moreover, when NPs constituting a layer must be analyzed comprehensively, the task becomes nearly impossible by using conventional methods. Optical methods, like the dynamic light scattering (DLS), are easy to handle, but do not produce highly resolved particle size distribution and do not provide shape information. Particles can be measured only in suspended form. Other sizing techniques commonly used for NP characterization like analytical centrifugation, small-angle X-ray scattering (SAXS) or fractionation methods (FFF) cannot be applied to NPs assembled into a dry film. Imaging techniques such as electron microscopies (SEM, TEM, TSEM) or atomic force microscopy (AFM) are the methods of choice when morphological characterization of single NPs assembled in a layer is requested. Direct imaging of particles enables the acquisition of accurate information about size, shape, crystallinity and elemental composition (latter by EDX) using different detection modes [11–13].

On-axis transmission Kikuchi Diffraction (TKD) on electron transparent samples in the SEM is a powerful technique, which can potentially meet these combined requirements. A high amount of forward scattered electrons is produced and disadvantages like high background intensity, beam broadening and insufficient Kikuchi contrast are considerably lowered, this leads to significantly higher spatial resolution than for conventional EBSD techniques [14–17]. Finally, TKD can be used to obtain information about NP particle orientation and phase as well as size and shape. Precondition is crystalline material prepared as an adequate thin sample of several tens of nanometers thickness. For TKD analysis various types of samples are suitable: isolated particles on an electron-transparent support, thinned specimens of the printed NP film using Focused Ion Beam (FIB) technique or electro-polishing [18]. In the literature, several TKD studies are dealing with precipitates or microstructural characterization of alloys [19–23], lithium distribution in electrodes [20] or cracking behavior in stainless steel [24]. To the best of our knowledge no systematic investigation on porous NP films was performed by means of TKD in a SEM up to now. In this study, we conducted on-axis TKD technique using a horizontal phosphor screen placed underneath the sample; the most intense, transmitted signal is detected to capture patterns (TKP) with minimal distortions. Spatial resolution can be further increased and beam-induced specimen drift is lowered when probe currents are reduced. We present TKD analysis of a screen-printed TiO_2 NP film with the main objective to extract particle size and shape with statistical significance; we compare the results with TEM and AFM results [25].

Besides the characterization of NPs, in terms of connection/networking of NPs, the inner structure of the NP film features an important parameter for cell efficiency. More specific, the free surface area and open porosity of the film are the parameters of interest. Porosity determines the volume of the sensitizer solution, which can be potentially infiltrated within the titania film. Surface area determines the amount of sensitizer, which can be adsorbed at the pore walls within the film. Both film structural parameters are only available from the original, printed NP film, that means no scratching or dissolution of the layer's particles took place. Porosity on the nanoscale with sufficient spatial resolution can be measured by several methods, for example, adsorption techniques or tomography techniques. Nitrogen adsorption (also called BET method) and mercury intrusion are favorable to analyze porous material with a wide range of pore sizes. However, for a reliable measurement a minimum amount of 100 mg powdered material is required, which can be difficult to obtain for a layer in the sub-micrometer range. Only scratching off the film from a large area of substrate and destruction of the original network results in an adequate amount of material for BET. This analysis procedure is just interesting for unprinted NPs to check inner porosity of the particulate powder. Other techniques like ellipsometry [26], nano computer tomography (nano-CT) [27,28], X-ray techniques (XRF, EDX with SEM) [29,30] or FIB tomography are more suitable for the layer dissection. Nano-CT bases on X-rays transmitting through a thin sample as well as the SEM/EDX approach bases on use of dedicated (commercially available) thin film analysis software. FIB is a milling technique conducted slice-per-slice with repeating SEM imaging of the manufactured cross-sectional surface [31,32]. By following reconstruction of certain parts of the investigated volume, layer parameters like porosity or surface area can be calculated based on the knowledge of the calibrated voxel size. Wargo et al. published detailed comparisons of nano-CT and FIB tomography for a porous material and emphasized the analytical strength of both techniques for the investigated material system: large-area, non-destructive investigation with nano-CT, but better spatial resolution in smaller investigation volumes for the FIB tomography [33,34]. Since our study is carried out on micrometer thick films and not on bulk material, high-resolution SEM micrographs are favorable to capture all pores within the layer thickness. The abundance of publications about FIB tomography highlights their application variability: microstructural characterization of alloy [35], the localization and quantification of precipitates [36], pile-up investigation from nanoindentation [37], morphologic study on nano-rods and nano-filaments [38,39] or reconstruction of porous networks of solid oxide fuel cells or batteries [40–46]. From these reports, also the large variety in processing of the resulting was ascertained. The experimental part follows as a routine procedure, however, the analysis of the image stack by image adjustment, binarization and reconstruction follows different routes. Within our study, we discuss the different approaches with respect to applicability to our scientific purpose.

In the end, a complete routine analysis procedure of thin films assembled from NPs is offered, including recommendations for the several employed techniques.

2. Experimental

2.1. Material and Sample Preparation

Thin TiO_2 NP films were fabricated by means of screen-printing of a NP ink onto fluorine doped tin dioxide (FTO)/glass substrates by Solaronix SA (Aubonne, CH). The TiO_2 NPs are well characterized as single crystalline anatase with bi-pyramidal shape. A detailed investigation on these particles well suited as a candidate for a reference material is provided elsewhere [22,25,47]. A representative image of the particles is presented in Fig. 1.

Using these TiO_2 NPs as a starting material, a paste with organic additives was prepared for screen-printing of the particles onto a typical clear float glass substrate coated with an electrically conductive FTO layer. The layer system was heated for calcination and a porous network structure has been formed. Two types of screen-printed TiO_2 layers were investigated: a 5 μm thick layer for the TKD study and a 500 nm thin layer for FIB tomography. For TKD and TEM measurements an electron transparent sample, i.e. a lamella of about 100 nm thickness, was prepared using conventional FIB machining with Ga liquid metal ion source (LMIS) from FEI company (DualBeam Quanta 3D FEG). Amorphisation and ion implantation was minimized during the thinning-down process using a decreasing acceleration voltage from 30 kV to 2 kV [48]. As a final polishing step, the sample was showered with low-voltage argon ion beam using the Fischione 1040 NanoMill® at Fischione instruments facility located in Export, PA, USA. This step was found out to be the best solution for obtaining ultrathin and defect-free samples with maximum 2–3 layers of grains.

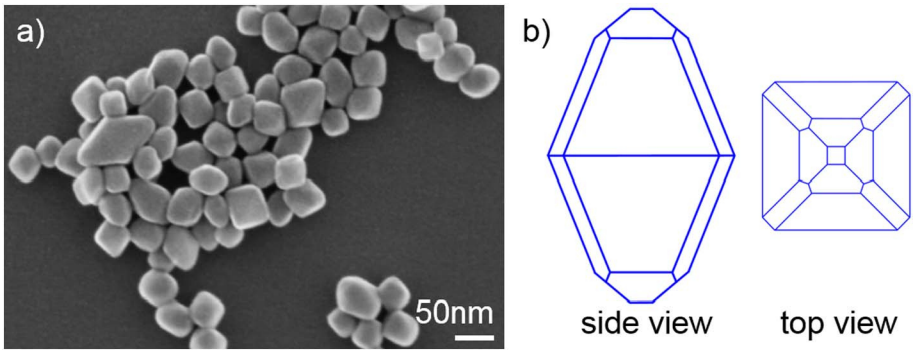

Fig. 1. a) SEM micrograph of the starting TiO_2 NPs as prepared on a silicon substrate, b) detailed schematic of the NPs shape, identified using high-resolution TEM (see later).

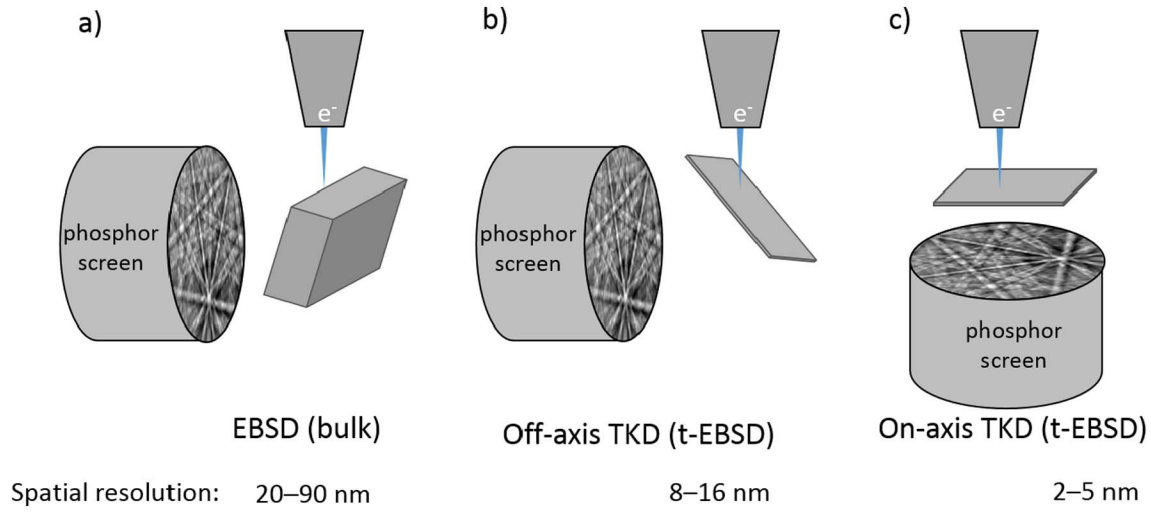

Fig. 2. Influence of the set-up onto the spatial resolution when detecting Kikuchi bands: a) conventional EBSD on bulk samples in reflection mode, b) using electron transparent samples tilted in a certain angle to the phosphor screen, and c) when electron beam, electron transparent sample and phosphor screen are aligned along one axis.

2.2. Characterization of TiO_2 NP Size and Shape

2.2.1. On-axis TKD

The detection on Kikuchi pattern can be realized on different ways as depicted in Fig. 2. Conventionally, the crystal's information is received from backscattered electrons diffracted on the lattice of a bulk material (Fig. 2a). Reduction of the interaction volume improves the spatial resolution, because beam broadening is lowered. Optimum results are achieved using an arrangement with electron beam, sample and phosphor screen in one line, called on-axis TKD (Fig. 2c). This small adjustment in comparison to off-axis TKD (Fig. 2b) improves the spatial resolution further. On-axis TKD was conducted by Bruker Nano GmbH (Berlin, Germany) using a Zeiss Merlin Compact SEM and the newly developed e-Flash^{FS} EBSD detector retrofitted with the OPTIMUS™ TKD detector head. This sort of detector is a very sensitive system allowing fast TKD measurement up to 660 frames per second. In our case, 3 ms exposure time was used to examine large areas with up to 250 frames per second. Step size was set to 2 nm and 3 nm and the pattern resolution to 320 × 240 pixels. Grains were distinguished when a misorientation of at least 5° was detected to separate single NPs with slightly different orientation. Incomplete grains were disregarded. From this type of measurements orientation mapping as well as grain, i.e. NP, size distributions were extracted.

2.2.2. Reference Methods: TEM, TSEM, AFM

To validate the results derived by TKD, conventional SEM (Zeiss 'Supra 40', Oberkochen, Germany) and TEM (JEOL JEM 2200 FS) have been used to analyze the shape and the connectivity between single TiO_2 NPs. More information on NP shape has been obtained by correlation of surface sensitive SEM (by In-Lens mode) with transmission mode at SEM (TSEM) for same scanned sample area. This type of quantitative dimensional investigation has been successfully demonstrated recently on other reference nano-particulate systems [12,49]. Additionally, AFM (Park Systems "NX20", Suwon, Korea) was also implemented on single particles to cross-check the dimensional results obtained by electron microscopy techniques on the same NPs. The AFM, a linearized 100 μm × 100 μm xy-piezo translation stage decoupled from a 10 μm z-scanner, has been applied in intermittent scanning mode. The "super-sharp" AFM tip (typical tip radius < 2 nm, half cone angle < 10°) oscillated close to its resonance frequency of approx. 330 kHz, and, thereby, the specimen was scanned without lateral forces.

3. Determination of Porosity and Surface Area

3.1. FIB Tomography

3.1.1. Preparatory Work

Once the TiO_2 NP starting powder was analyzed with respect to size and shape of its constituent NPs but also to its porosity, the resulting screen-printed layer was characterized using FIB tomography. Fig. 3 visualizes schematically the main steps of the complete procedure. The process starts with the selection of an appropriate region of interest on the TiO_2 layer and the definition of a statistically representative slicing volume. For the on-hand sample the layer thickness of 500 nm to 600 nm is the limiting factor in y-direction (see Fig. 3). The width (i. e. x axis) and the depth of the volume (i.e. z axis), which is subdivided in slices with certain distance, are arbitrary. Based on the theory of the Representative Volume Element (RVE) described by Joos et al. a width of 5 μm (x) and depth of 10 μm (z) were fixed [34,42]. They stated that

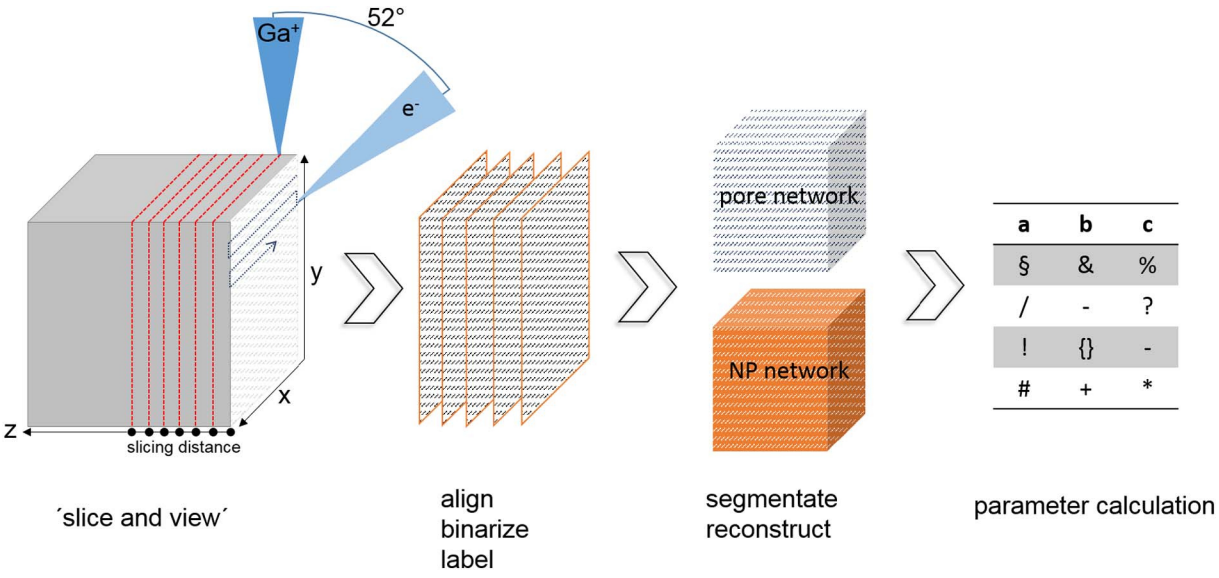

Fig. 3. Scheme of the FIB tomography sequence. Process starts with milling (with Ga^+ ion beam) of slices with certain thickness in a pre-defined sample volume. After each slicing step a high-resolution SEM micrograph is recorded at 52° due to the FIB set-up. Image stack is aligned, binarized and voxels are labeled either as 'pore' or 'NP'. Next, segmentation follows with subsequent reconstruction of the labeled phases. Parameters like surface or volume can be extracted for the phase of interest.

10–15 voxels per particle are needed to obtain reliable reconstruction results. With the set resolution of 2.9 nm in x and y direction and 30 nm as slicing distance, this pre-condition is partly fulfilled.

Before slicing, a thin layer of platinum was deposited onto the sample surface using the chemical vapor deposition system within the FIB instrument. A platinum protective cap layer leads to a smoother milled surface and its presence avoids the so-called 'curtaining effect' induced by the surface roughness. The curtaining effect is a FIB milling artefact appearing as narrow channels/stripes along the ion beam direction. In result, obstructive shadowing effect becomes clearly visible in the SEM micrograph, see Fig. 4a. Strongly different milling rates in the sample caused by different material densities (e.g. hard/soft; material/pore) and a rough surface enhances this effect. To circumvent curtaining, the porous sample can be embedded into an epoxy resin by means of vacuum impregnation. This procedure was tested here using a liquid resin 'M-Bond 610' typically applied for TEM samples. A drop of about 10 µL was placed on the sample; afterwards, the air within the pore network was evacuated for 2 min to allow infiltration of the bond into the pore structure. This hollow space of pore network was filled completely; corresponding milled surface of the sample does not exhibit curtaining anymore, see Fig. 4b. However, after this type of sample preparation, the pore boundaries appear washy in the SEM micrograph and the insufficient contrast becomes an issue especially for smaller pores. We decided to renounce to the use of resin for fine-pored materials. A conductive embedding material would be more suitable here. This aspect must be checked systematically for future experiments. Pores larger than about 200 nm should be filled with resin and the view into the interior of the layer is obstructed (see Fig. 4a, red line). The inner structure of the great pore is visible, but the information in these pixels does not belong to the actual slicing plane. In the following semi-automatic reconstruction step this image information is interpreted erroneously.

3.1.2. FIB Slicing

The material around the defined volume was excavated in form of grooves with 8 µm depth and 15 µm width to avoid any shadowing effects from side walls, and to prevent the milled surface from re-deposition. A marker represented by a ring is milled next to the region of

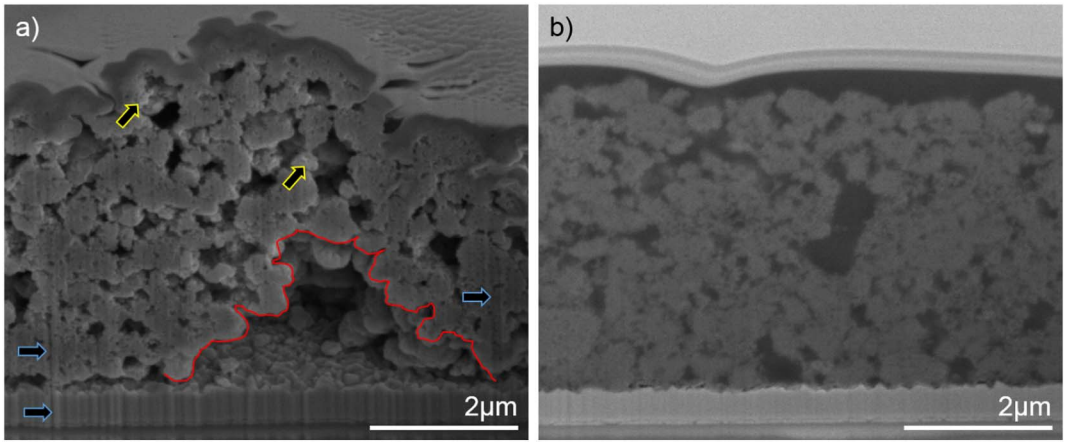

Fig. 4. Example for porous TiO_2 material: a) SEM micrograph of un-embedded TiO_2 NP layer shows very good contrast, but also artefacts like curtaining (blue arrows) and charging at pore boundaries (yellow arrows). During the automatic image post-processing step, the determination of the true pore rim (red line) becomes impossible due to the view into the interior of the pore. The light grey pixels within the pore will be assigned to bulk material within this slicing plane, b) embedded (with resin) structure presenting a smooth surface without curtaining effect, without charging and without visible material (see grey pixels) belonging to other slicing planes (no grey value distribution within the area of one pore). Image lacks sharpness at pore boundaries, which becomes critical for very small pores. (For interpretation of the references to colour in this figure legend, the reader is referred to the web version of this article.)

interest for identification and alignment of the ion beam during the process. The slicing distance (see Fig. 3) was set to 30 nm using an acceleration voltage of 30 kV and an aperture corresponding to a beam current of 0.3 nA. These parameters were found as the optimum with respect to clean surfaces with minimum curtaining and re-deposition effects. Setting the appropriate optimal slicing distance is always a trade-off between instrument capabilities regarding beam stability and as small as possible slicing pattern, time which can be invested in experiment, data analysis, and spatial resolution. 30 nm are in this case a compromise, since the particles are about 50 nm in size, but pores can be much smaller, of course. This uncertainty source must be considered in following calculations. After each slicing event, a 2D SEM image was recorded with a resolution of 2.9 nm pixel size in both x and y directions. The whole slicing and imaging process took about 10 h with a result of 490 images.

3.1.3. Data Analysis

Next step is the alignment of the images. In this case an automatic y-shift correction during the slicing process was available. Due to the automatic option, the image stack is pre-aligned and only small misalignment due to beam drift or sample drift must be corrected after slicing. Here, we used the commercially available software Amira (FEI company, USA). Further, images were scanned by the electron beam under an angle of 52° to normal axis, while sectioning was carried out perpendicular to the sample surface. The images were corrected for this angle and due to this voxel sizes (a pixel in 3D) change to x = 2.9 nm, y = 3.7 nm and z = 30 nm. In some cases, further image processing is necessary to subtract gradients [32,48] or curtaining [50,51]. Since the layer under study was only 500 nm thick, a gradient was not present and curtaining was manageable, so that these types of processing were not necessary to be applied. Filtering always changes image information and must be used with special care. Next step is the thresholding necessary for binarization of the images. Two options are available: the global or local method. Global thresholding makes sense when the image exhibits a distinct bimodal grey scale distribution, which is often not the case in multi-component materials with overlapping grey scales in the image histogram. Fig. S1 (in the supporting information section) shows several local thresholding results when processing with the freeware software package ImageJ [52]. Using the local methods, the threshold is computed for each pixel in correlation to the pixels around within a given radius. Fig. S1 shows the best match results for the current thresholding methods of Otsu [53], Sauvola [54] and Phansalkar [55].

Another solution would be the use of ISODATA algorithm [56]. A general recommendation with respect to finding the ´true´ structure of the sample is not possible. Thresholding constitutes a crucial step for accurate quantification of layer porosity bearing mostly the highest uncertainty potential. The applied algorithm must fit to the present study. For instance, the Phansalkar algorithm with radius of 15 pixels gave to our findings the best match concerning the pore identification, localization and filling out of the inner pores, although some pore boundaries in the SEM images are diffuse. The Phansalkar method was developed originally to detect tiny dark cells and nuclei in light microscopy images of biological histologic samples, which are often influenced by staining and, thus, contrasts are smeared or diffuse as in our present case. Further processing using Maximum filter (1 pixel) and a second Median filter (1–2 pixel) was applied. The segmentation was carried out using the Amira software package and its built-in tool for reconstructing the 3D pore network. Now voxels can be counted for each phase and, eventually, volume and surface information can be extracted.

3.1.4. Reference Method: Isothermal Sorption of Vapors at Solids

For the independent determination of the porosity by means of sorption of vapors at solid's surface, the calcinated TiO_2 layer was scratched off from the glass substrate. The resulting powder was measured using the nonpolar octane as well as the polar water as adsorptive. This method is a gravimetric technique useful to study the adsorption behavior of materials at room temperature [57]. Two cups with sample powder are purged with nitrogen, while one of the sample acts as a reference and is just treated with dry gas. The other sample is treated with gas loaded with octane or water with continuously increasing concentration until the adsorptive maximum is reached. This state is hold and reversed afterwards. The specific surface area is calculated from the amount of adsorbed octane/water on the TiO_2 surface. This method is an indirect technique and its result is extremely influenced by the chemical environment on the NPs surface.

4. Results and Discussion

4.1. Particle Size and Shape

To measure size and shape NPs are analyzed mostly by TEM or high-resolution (T)SEM [58,59]. The analysis is time-consuming. The sample preparation is a great challenge, since the particles must be well-dispersed, ideally isolated, on a substrate (bulk or support membrane).

The size and shape parameters evaluated for the identified NPs in T(S)EM and AFM are listed in Table 1. Representative images are presented in Fig. 5a and c.

The AFM analysis of a single TiO_2 (laying) NP as shown in Fig. 5b indicates measured particle length and width of 78 nm × 56 nm as mean values. The overestimation of approximately 16–20 nm on both particle dimensions compared to TSEM measurement is mainly caused by the finite dimensions of the probing tip. The tip radius alone dilates the particle shape by 2 nm on either side of the particle. The half cone angle of 10° adds again approximately 6 nm for a 34 nm high particle on either side, resulting in a total dilation of approximately 16 nm. The remaining difference can be emerged by an overestimation of the

Table 1
Measured TiO_2 NP dimensions.

Technique	Nr. of particles	Mean Feret max/nm	Mean Feret min/nm	Mean shape factor[a]	Mean equivalent circular diameter/nm[b]
TSEM	204	50 ± 9	32 ± 5	0.64	40 ± 7
TEM	2	53	34	0.64	41
AFM (single particles)	3	78	56	0.72	66
AFM (layer surface)	100	73.5 ± 11.3	48.5 ± 7.6	0.66	55.5 ± 7.6
TKD	1839	60 ± 6[c]	39 ± 3[c]	0.65	43.8 ± 5
TKD - including orientation[d]					
[100]	236	51 ± 6	30 ± 3	0.58	39 ± 5
[110]	162	50 ± 6	26 ± 3[e]	0.52	38 ± 5

[a] Ratio of Feret min to Feret max.
[b] Based on fitted ellipses to NPs with Feret min and Feret max as axes.
[c] Calculated from shape factor and equivalent circular diameter.
[d] As described in text and Fig. S2.
[e] Calculated from original value of 37 nm for the diagonal axis of the quadratic base area using Pythagoras' theorem.

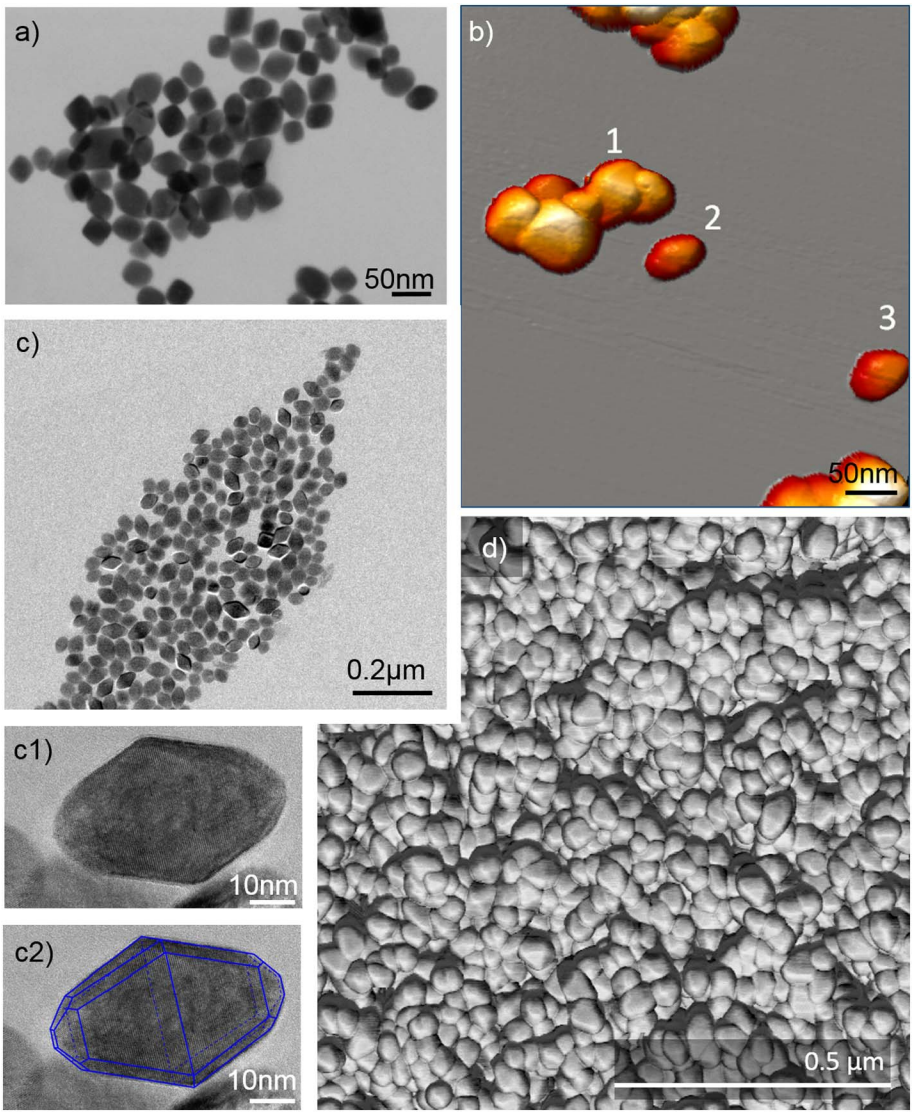

Fig. 5. Particles of the TiO_2 starting powder prepared on carbon TEM grid and mica (for AFM), imaged with a) TSEM, b) AFM, and c) TEM overview: c1) single particles with visible lattice planes, c2) extracted shape with measurable dimensions, d) AFM image of a surface of a NP layer.

particle shape using the edge detection procedure, which may add one or two pixels, corresponding to 2 nm or 4 nm respectively. The AFM analysis of the surface topography of the nano-particulate layer, Fig. 4d, as used for the following TKD study, is in good agreement with the TSEM results.

An analysis of individual NPs within (through the depth of) a calcinated TiO_2 NP layer, that means the final product, is hardly possible with these techniques, because assembled particles lay on each other and cannot be distinguished. Fig. 6a shows an TEM image of a part of a FIB milled electron transparent lamella prepared from TiO_2 NP layer system. Fig. 6b shows single NPs as well as their inter-connection; however, the NPs cannot be observed completely isolated, because across the thickness of the lamella several particles are stacked over. Distinction between certain particles is a time-consuming and laborious

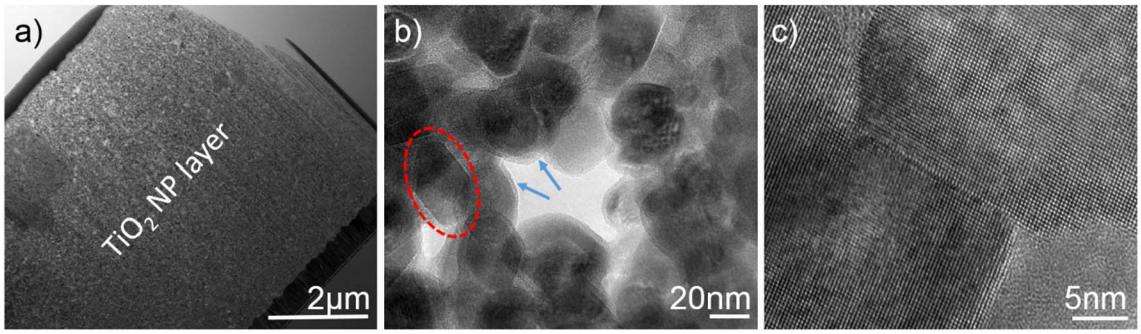

Fig. 6. TEM images of a screen-printed TiO_2 NP layer infiltrated with a Ru-sensitizer: a) lamella of the 5 µm thick layer (here FIB milled sample with protective Pt coating), b) higher magnification of the layer, red dotted particle indicates the bi-pyramidal shape; the NPs are stacked and therefore it is hardly possible to identify them accurately for size measurement; blue arrows present an amorphous coating on the particles as expected after infiltration with sensitizer, (c) isolated particles in high-resolution mode, when the single crystalline character of the particles becomes visible. (For interpretation of the references to colour in this figure legend, the reader is referred to the web version of this article.)

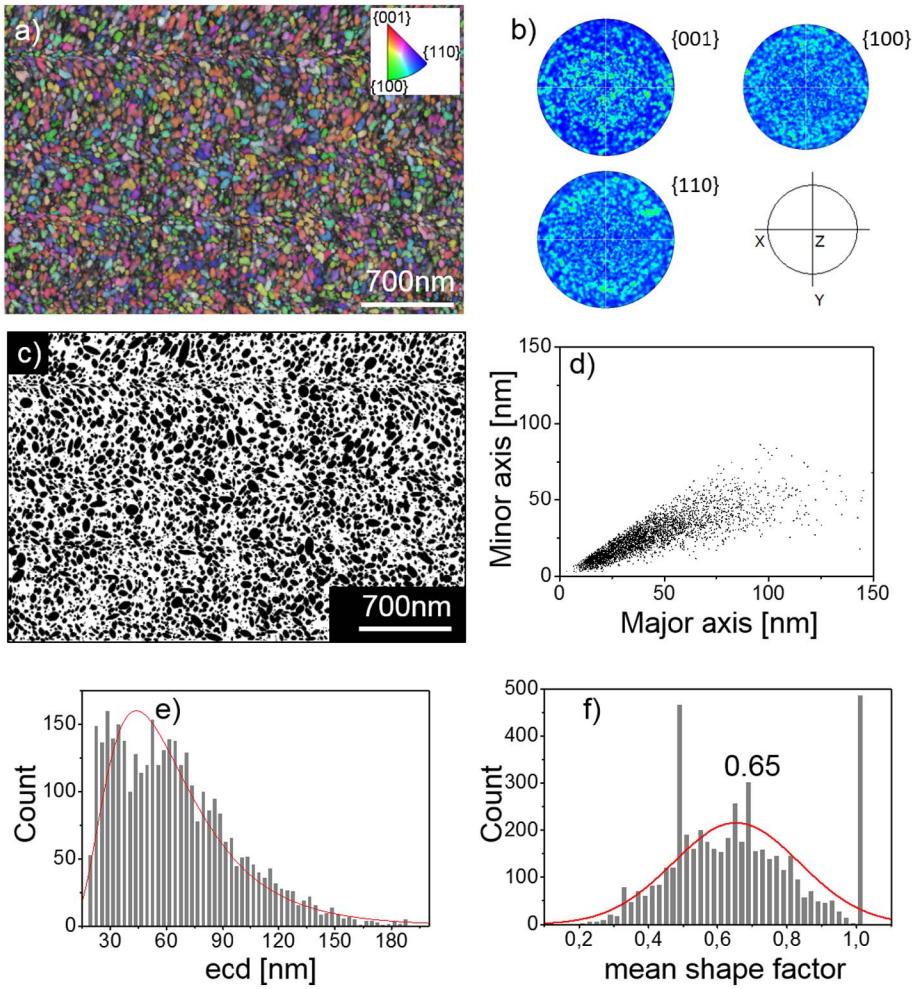

Fig. 7. TKD analysis on a FIB lamella prepared from TiO_2 NP layer: a) inverse pole figure map in z direction, black areas represent pores, b) pole figures show slightly preferred orientation of NPs in {001}, c) fitted ellipses (in black) to the indexed grains after processing with ImageJ, d) minor and major axes plot of the fitted ellipses from c), e) corresponding log-normal shaped distribution of the equivalent circular diameters (ecd) of ellipses with maximum value 48.3 nm, f) normal shaped distribution of mean shape factor of the ellipses with maximum value of 0.65. The distributions are not useful for the determination of particle Feret min and Feret max, because NPs are oriented arbitrary in all directions.

effort. In Fig. 5c and 6c the crystallinity of the single particles is proved using high-resolution TEM, which is precondition for the successful application of the TKD technique.

Fig. 7a provides a large area orientation map of lamella measured with on-axis TKD with high spatial resolution (3 nm pixel size), so that 1839 grains could be detected by only one measurement. Nevertheless, the map was affected by beam jumps stemming from beam instabilities or charging of the material visible as elongated, very small and ranged grains. Within the post-processing of the data we found that exclusion of the drifted parts of the map has no significant influence on the overall result. Routinely, very small NPs (consisting of four pixels) are excluded from evaluation, because they may be truncated by FIB milling or deformed by beam drift and do not represent true entire particles.

According to the pole figures in Fig. 7b, as expected, the particles are not arranged in a preferred orientation, just a slight preference is noticed in {001}. This means that the map shows NPs in various positions in free space. The projection of these grains ideally should be associated to the minimum and maximum length of the single NPs. Fig. 7c presents the same map as depicted in Fig. 7a, but here grains are fitted to ellipses using the open software ImageJ and its plugin 'analyze particles'. The corresponding minor and major axes are represented in Fig. 7d. Most data points are concentrated between 3 nm and 60 nm for major axis and between 3 nm and 50 nm for the minor axis. Data points above 100 nm for major axis represent deformed, elongated grains generated by drifting effects. Similarly, the very small grains - we suggest below 12 nm (4 pixel) in major and 9 nm (3 pixel) in minor axis - should be neglected, because of truncation by FIB milling. Fig. 7e presents the calculated equivalent circular diameter as log-normal distribution with its maximum at 48.3 nm. By calculation of the aspect ratio (ratio of minor axis to major axis) a normal distribution is produced with the maximum at 0.65 (see Fig. 7f). The high population with aspect ratio of 1 (equal minor and major axes) may be attributed to the particles in [001] orientation, which was ascertained to be slightly preferred. High NP number at around 0.5 might be due to a fraction of NPs, where major axis is two times larger than the minor axis. It is not explainable by a certain orientation of the particle.

Noteworthy is that information about the relevant parameters Feret min and Feret max of the single particles are not available by consideration of all NPs, because of their random orientation distribution. By means of high resolution TEM it was possible to extract orientations for which the particle parameters of interest are fully accessible. Specifically, the [100] and [110] orientations (Fig. S2a and S2d in the supporting information section) provide Feret max and Feret min (here identical with major axis and minor axis) of the fitted ellipses, while a [110] oriented NP is 'just' a [100] oriented NP rotated 90° around its long axis. [100] oriented NPs are in Fig. 7a - with respect to the inverse pole figure map - all green colored particles. Using ImageJ all green particles (roughly all particles from light green to turquoise) were selected (Fig. S2b) and ellipses were fitted to them. The corresponding major and minor axes histogram is plotted in Fig. S2c. Assuming a normal distribution the mean major axis was 51 nm and mean minor axis 30 nm. Similar results were found using Bruker ESPRIT 2.1 software analysis for identification of the colored particles instead of the ImageJ software. The same procedure was applied to the [110] oriented NPs corresponding to all 'blue' colored grains (ranging from turquoise to violet) in Fig. S2e. Here the maxima reveal 50 nm for major axis and 37 nm for minor axis as shown in Fig. S2f. The minor axis of the fitted

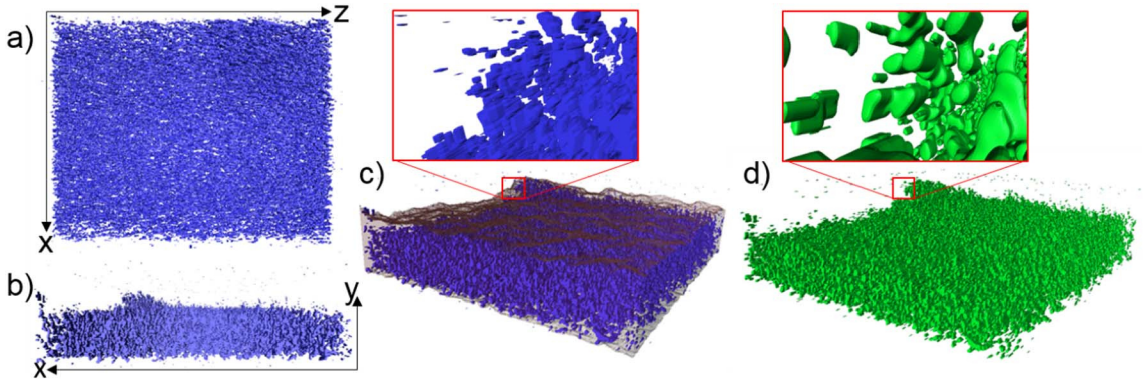

Fig. 8. Reconstructed pore network of a part of a TiO_2 NP layer (sampling size was x = 3.2 µm; y = 1.1 µm; z = 4 µm): a) xz view onto the pore network, b) xy view onto the pore network, c) tilted view with TiO_2 in transparent and magnified view onto the pore surface (see explanation in text); voxel size for a), b) and c) is 2.9 nm × 3.7 nm × 30 nm, d) re-sampled pore network with voxel size 2.9 µm × 2.9 µm × 2.9 µm.

ellipses for the blue colored NPs represents the diagonal length of the squared base of the bipyramidal shaped NPs. Therefore, it is marked as minor axis* in the diagram. Using Pythagoras` theorem the true minor axis accounts to 26 nm. The fit of a normal distribution function was not completely satisfactory in this case. Within the selection of the colored particles all tones of green or blue pixels were considered, meaning that part of the NPs is slightly rotated. The percentage of individual green or blue toned pixels (i.e. the different rotations) is random and does not lead automatically to a normal distribution of the axis lengths. The dimension of major axis is more affected by rotation and thus its distribution is more spread than for minor axis distribution. One way out is to select only pixels with certain green or blue tones corresponding to 100% [100] or [110] oriented NPs, respectively. Consequently, the number of selected particles decreases considerably. Application of this special case results in minor axis-major axis plot in Figs. S2g and S2h. Most values are concentrated between 0 nm and 25 nm. We assume that these particles are truncated. The largest values of major and minor axes equalize the Feret max and Feret min of the single NPs (without necessarily knowing if these particles are also truncated). The values for the major axis account to 60 nm to 70 nm for both orientations. The shorter axes can be defined as 35 nm to 45 nm for the [100] oriented NPs and 45 nm to 55 nm for the diagonal axis of [110] oriented NPs, which gives 32 nm to 39 nm after calculation back to the square profile. In comparison with the results of other analytical techniques these values are quite similar, but can be extracted only for a reduced number of single particles. Moreover, TKD analysis can be performed with a high-quality FIB sample and several mappings are conducted. The number of particles with favorable orientation becomes larger and a more statistical analysis can be initiated. The acquisition time ranges between 20 and 60 min per map.

According to the procedure described above, TKD analysis includes also some pitfalls which must be considered. First issue is the edge-gating of the single particles using FIB, because their projected area is smaller than the projected area of intact NPs. Since the TKD signal stems from the last nanometers underneath the bottom surface of the lamella, the influence of FIB truncated particles onto the resulting NP size distribution is rather high. If the interesting parameter is length of individual particles, we suggest to measure isolated particles on TEM grids as it was proceeded for T(S)EM analysis. However, if the constitution and orientation of particles in layer are of interest, the described method by FIB preparation will constitute the preferred option.

Second issue refers to the micro-structure of the sample. The indexing rate reflects the porosity of the sample. Brodusch et al. stated that emerging electrons may be absorbed at the pore rims and thus diffraction signal is vanished [15]. Indeed, we found that the indexing rate at the particle boundaries is lower. The NPs in the present study are surrounded by ruthenium-complex sensitizer. Due to their amorphous character, this thin shell surrounding the TiO_2 NPs may affect the indexing success. One solution is to leave the sensitizer; second solution would be to embed the particles into matrix. The detailed description is given in Section 3.1.1., where conductive embedding material should be preferred.

To summarize the TKD analysis, the proof-of-principle of the application of TKD on size and shape measurement of NPs constituting the TiO_2 film is validated. Information on orientation and aspect ratio of the single NPs are directly accessible from the recorded inverse pole figure maps as well as rough size of the NPs. Sensitive parameters like major and minor axis dimensions of the entire NPs are accessible via selection of favorable oriented NPs from the inverse pole figure map.

4.2. Porosity and Surface Area

With respect to the capacity of the porous TiO_2 NP layer, which is infiltrated with the ruthenium dye complex, the true structure of the pore interconnection within the TiO_2 matrix layer is of crucial importance in terms of quantification. From BET measurements of the starting TiO_2 powder no inner porosity of the particles was detected. Only pores in between the particles assembled within the screen-printed layer must be considered in the following tomography study. Fig. 8 shows the reconstructed pore network. As expected, the pores are elongated in z direction since the slicing distance of 30 nm was rather high. Whenever a pore voxel meets another pore voxel in the next slicing level at the same location, the pores were connected to each other by the reconstruction software and appear consequently as one elongated pore. The real structure in between the slices cannot be reproduced perfectly and the reconstruction should be considered as a rough estimation of the real structure. The detailed description of Jones et al. warns of additional pitfalls [60]. They showed that also the slicing distance itself can be affected by an uncertainty of 20% near the surface of a sliced volume, in depth (y direction) this error even increases up to 60%. We specify the true slicing distance in the present work as 30 nm having associated an uncertainty of ± 6 nm.

Using the built-in tool of Amira software package, it is possible to count the voxels within the pore volume as well as to measure the surface area of the pores and TiO_2 matrix material, respectively. This was performed using a triangular approximation, which means the generation of a mesh of triangles covering the selected voxels. The area of each triangle is easy to read out for the program and, by adding all triangle areas, the overall surface area is calculated. The values for the calculated characteristics can be found in the Table 2.

A layer porosity of 11% was found, which is very small compared to 70%–80% porosity calculated by Gan et al. for similar shaped particles, which were of larger size (micrometer-sized) in loose packing [61]. These authors found out that any deviation from spherical shape increases the porosity of the whole system. Furthermore, size of the particles is a factor for the packing density. The smaller the particle the

Table 2
Calculated characteristics of porous TiO_2 NP layer.

Parameter	FIB tomography		Dynamic vapor sorption	
	Raw voxel size x(2.9 nm)Y (3.7 nm)Z (30 nm)	Re-sampled x = y = z (2.9 nm)	With octane	With water
Total volume (pore + TiO_2) [μm^3]	8.55	8.55		
Pore volume [μm^3]	0.92	1.38		
Porosity[a]	0.11	0.16		
Surface area [μm^2]	166	220		
Volume specific Surface area [μm^{-1}]	19.4	25.7	115.6[b]	104.6[b]
Specific surface area [$m^2 g^{-1}$]	4[b]	5.4[b]	25.1 ± 2	21.8 ± 2

[a] Pore volume/total volume.
[b] Calculated with $\rho = 4.8\ g\ cm^{-3}$.

more non-contact van-der Waals forces dominate the particles mobility and determine their final position. This effect increases the porosity of the system. Since their smallest particles studied exhibit diameters of 2 μm, a prediction to nano-sized particles has proven as difficult. Besides particle properties, also the deposition method and its treatment afterwards affect the packing density of the system [62]. Printing intensity, velocity as well as the viscosity and degree of wettability for the ink paste added to the starting dry TiO_2 NPs are other factors which can lower significantly the layer porosity. At least, a certain part of connected open pores must be available to enable a uniform flow of the Ru-complex-sensitizer liquid through the entire layer matrix. The minimum amount of such pores must be investigated in DSSC efficiency tests.

Further, the inner surface area is another relevant parameter, because sensitizer molecules cover the particles for the photo-electrochemical reaction. The accessible space in the inner of the porous layer determines the maximum amount of sensitizer can be infiltrated and, finally, the efficiency of the DSSC.

With BET adsorption method, a specific surface area of 52.2 $m^2 g^{-1}$ was measured for the TiO_2 starting powder containing unconnected particles in loose packing without any additional paste or dye in between. The measurement of the screen-printed layer via octane and water vapor adsorption gives a value of about 21–25 $m^2 g^{-1}$, which is nearly half of specific surface area of the un-assembled particles. In contrast, FIB tomography leads to a value between 4 $m^2 g^{-1}$ and 5.4 $m^2 g^{-1}$ (using a density value of 4.8 g cm^{-3} for anatase), which is significantly lower than that obtained by the adsorption method. The difference can be explained by consideration of the methods limitations. Vapor adsorption was measured on scratched material, that means the original network is partly broken so that additional surface for adsorption is generated. On the other hand, closed pores cannot be considered. The percentage of both issues to the true specific surface area is unknown. However, FIB tomography can catch open pores as well as closed pores, but resolution is limited. Smallest nano-pores below 30 nm in z and about 10 nm in x and y couldn't be accessed here. Better contrasts and thus a more accurate classification of voxels as part of the binarization sequence may be obtained by infiltration of conductive material filling open pores completely. In consequence, it might be possible to decrease the slicing distance, too. Nevertheless, the true value for specific surface area is estimated somewhere in between the results obtained with the two techniques. Finally, we assume the data obtained from FIB tomography as being more reliable, because measurement was conducted on the original coating layer.

Joos et al. recommended to re-sample the voxel size, that means to re-shape the asymmetric voxels into cubic ones by keeping the same volume [42]. This is needed whenever the voxel size is not the same in all directions and specific parameters are extracted [63]. In our study, we would refine the slicing distance down to a voxel size of 2.9 nm. During resampling sequence the software generates new voxels in z direction when going from one slice to the next. To obtain a reliable surface area estimate, according to Wargo et al., features with diameters of 20 to 30 voxels are necessary [33]. However, the values for porosity and surface area have changed after resampling, because the surface is approximated in a different way compared to the reconstruction with the raw voxel size. In comparison to non-resampled data the porosity and surface area are larger. This proves how sensitive are the data to such processing steps. Such resampling demonstrates an example for software-only manipulation. We suggest to conduct resampling only when voxels are coarsened (i.e. adding several real voxels to one larger voxel) rather than voxels to be refined (i.e. abstracting from one voxel to several smaller voxels).

Recapitulated and in agreement with Taleb et al., a film with such a low specific surface area with similar particle size would only achieve a middle efficiency [10]. The tests in the present study were conducted with irregular shaped particles and the influence of the bipyramidal shape on the DSSC's efficiency is not known yet. The authors in [10] stated that superior performance of corresponding DSSC would be reached by aggregation of several TiO_2 NPs forcing the inner porosity to balance out requirements of high surface area, good connectivity for charge transport and enhanced light scattering.

5. Conclusion

A combined methodical approach applied as detailed characterization of the inner structure of screen-printed, porous TiO_2 NP films has been successfully demonstrated as a proof-of-principle. Visualization of 3-D network of the pores within the TiO_2 NP layer matrix, but also quantitative information about inner surface area and porosity of the nanoparticle film are possible to be extracted after discrete slicing by focused ion beam (FIB) and 3-D image reconstruction of the sequentially collected SEM micrographs. The limitations of the FIB tomography with respect to the detection of pores below the spatial resolution of the method are discussed. Verification of the results has been using traditional adsorption measurements; however, it is difficult to apply, since only low amount of film is available for this type of model samples. Other analytical techniques could not be considered for this analytical task due to surface roughness (ellipsometry) or too complex substrate structure (FTO layer on glass) for X-ray spectroscopies. Solutions for enhancing the image contrast, for instance, use of a more appropriate resin or use of high(er)-resolution SEM for the sequential imaging will be pursued in the future. Recently developed transmission Kikuchi diffraction (TKD) technique employed within a SEM on electron-transparent lamellae has been found as conclusive - also quantitatively - in terms of determination of size and shape distribution of grains, in our case anatase nanoparticles, as they are assembled within the porous TiO_2 layer. The quantitative results have been validated by independent measurements performed by electron microscopy on individual NPs, but also by AFM applied on both NPs in the starting powder and on the sample surface of the TiO_2 layers. Summing up, the novel methodical approach of combination of FIB tomography with TKD has been proved to be a unique analytical tool to characterize challenging morphological parameters of porous films, which are decisive for solar cell performance, like surface area and 3-D pore distribution within the TiO_2 film matrix.

Acknowledgements

This work was supported by the SETNanoMetro Seventh Framework Programme project (project number 604577; call identifier FP7-NMP-2013_LARGE-7). Thank you to Prof. Valter Maurino (University of Torino) for sample preparation and to Mr. Carsten Prinz and Ms. Annett Zimathies (BAM) for the adsorption measurements.

Appendix A. Supplementary data

Supplementary data to this article can be found online at http://dx.doi.org/10.1016/j.matchar.2017.06.030.

References

[1] B. O'Regan, M. Grätzel, Nature 353 (757) (1991).
[2] J. Gong, J. Liang, K. Sumathy, Renew. Sust. Energ. Rev. 16 (2012) 5848.
[3] J. Gong, K. Sumathy, Q. Qiao, Z. Zhou, Renew. Sust. Energ. Rev. 68 (2017) 234.
[4] Y.K. Eom, S.H. Kang, I.T. Choi, Y. Yoo, J. Kimb, H.K. Kim, J. Mater. Chem. A 5 (2017) 2297.
[5] A. Hegazy, N. Kinadjian, B. Sadeghimakki, S. Sivoththaman, N.K. Allam, E. Prouzet, Sol. Energy Mater. Sol. Cells 152 (2016) 108.
[6] S. Surya, R. Thangamuthu, S. Murugesan, S. Kumar, G. Murugadoss, Superlattice. Microst. 102 (2017) 424.
[7] N. Tasi, Z. Marinkovi Stanojevi, Z. Brankovi, U. Lančjevac, V. Ribi, M. Žuni, T. Novakovi, M. Podlogar, G. Brankovi, Electrochim. Acta 210 (2017) 606.
[8] S.K. Das, M.K. Bhunia, A. Bhaumik, Dalton Trans. 39 (2010) 4382.
[9] A.K. Patra, S.K. Das, A. Bhaumik, J. Mater. Chem. 21 (2011) 3925.
[10] A. Taleb, F. Mesguich, A. Hérissan, C. Colbeau-Justin, X. Yanpeng, P. Dubot, Sol. Energy Mater. Sol. Cells 148 (2016) 52.
[11] J. Mielke, S. Rades, E. Ortel, T. Salge, V.-D. Hodoroaba, Microsc. Microanal. 21 (Suppl. 3) (2015) 1713.
[12] V.-D. Hodoroaba, C. Motzkus, T. Macé, S. Vaslin-Reimann, Microsc. Microanal. 20 (2014) 602.
[13] C. Motzkus, T. Macé, F. Gaie-Levrel, S. Ducourtieux, A. Delvallee, K. Dirscherl, V.-D. Hodoroaba, I. Popov, O. Popov, I. Kuselman, K. Takahata, K. Ehara, P. Ausset, M. Maillé, N. Michielsen, S. Bondiguel, F. Gensdarmes, L. Morawska, G.R. Johnson, E.M. Faghihi, C.S. Kim, Y.H. Kim, M.C. Chu, J.A. Guardado, A. Salas, G. Capannelli, C. Costa, T. Bostrom, Å.K. Jämting, M.A. Lawn, L. Adlem, S. Vaslin-Reimann, J. Nanopart. Res. 15 (1919) (2013).
[14] R.R. Keller, R.H. Geiss, J. Microsc.-Oxford 245 (245) (2012).
[15] N. Brodusch, H. Demers, R. Gauvin, J. Microsc.-Oxford 250 (1) (2013).
[16] P.W. Trimby, Ultramicroscopy 120 (2012) 16.
[17] G.C. Sneddon, P.W. Trimby, J.M. Cairney, Mater. Sci. Eng. R 110 (2016) 1.
[18] W. Zieliński, T. Płociński, K.J. Kurzydłowski, Mater. Charact. 104 (2015) 42.
[19] M. Abbasi, D.-I. Kim, H.-U. Guim, M. Hosseini, H. Danesh-Manesh, M. Abbasi, ACS Nano 9 (2015) 10991.
[20] N. Mortazavi, M. Esmaily, M. Halvarsson, Mater. Lett. 147 (2015) 42.
[21] S. Birosca, R. Ding, S. Ooi, R. Buckingham, C. Coleman, K. Dicks, Ultramicroscopy 153 (2015) 1.
[22] A.A. Saleh, G. Casillas, E.V. Pereloma, K.R. Carpenter, C.R. Killmore, A.A. Gazder, Mater. Lett. 114 (2016) 146.
[23] D. Robert, T. Douillard, A. Boulineau, G. Brunetti, P. Nowakowski, D. Venet, P. Bayle-Guillemaud, C. Cayron, ACS Nano 7 (2013) 10887.
[24] M. Meisnara, A. Vilalta-Clementea, A. Gholiniab, M. Moodya, J. Wilkinsona Angus, N. Huinc, S. Lozano-Perez, Micron 75 (2015) 1.
[25] E. Ortel, L. Pellutiè, F. Pellegrino, V. Maurino, J. Mielke, B. Powierza, I. Häusler, W. Österle, V.-D. Hodoroaba, Microsc. Microanal. 21 (Suppl. 3) (2015) 2401.
[26] D.-M. Rosu, E. Ortel, V.-D. Hodoroaba, R. Kraehnert, A. Hertwig, Appl. Surf. Sci. (2017), http://dx.doi.org/10.1016/j.apsusc.2016.11.055 (in press).
[27] D. Attwood, Nature 442 (2006) 642.
[28] A. Sakdinawat, D. Attwood, Nat. Photonics 267 (2010) 840.
[29] B.M. Patterson, K.A. De Friend Obrey, C.E. Hamilton, C.E.G.J. Havrilla, X-Ray Spectrom. 41 (253) (2012).
[30] E. Ortel, A. Hertwig, D. Berger, P. Esposito, A.M. Rossi, R. Kraehnert, V.-D. Hodoroaba, Anal. Chem. 88 (2016) 7083.
[31] A.J. Kubis, G.J. Shiflet, D.N. Dunn, R. Hull, Metall. Mater. Trans. A 35a (2004) 1935.
[32] M.D. Uchic, L. Holzer, B.J. Inkson, E.L. Principe, P. Munroe, MRS Bull. 32 (2007) 408.
[33] E.A. Wargo, T. Kotaka, Y. Tabuchi, E.C. Kumbur, J. Power, Sources 241 (2013) 608.
[34] E.A. Wargo, V.P. Schulz, A. Çeçen, S.R. Kalidindi, E.C. Kumbur, Electrochim. Acta 87 (2013) 201.
[35] A.V. Nagasekhar, C.H. Cáceres, C. Kong, Mater. Charact. 61 (2010) 1035.
[36] S.S. Singh, J.J. Loza, A.P. Merkle, N. Chawla, Mater. Charact. 118 (2016) 102.
[37] B.J. Inkson, T. Steer, G. Moè Bus, T. Wagner, J. Microsc.-Oxford 201 (2001) 256.
[38] K.M. Krause, D.W. Vick, M. Malac, M.J. Brett, Langmuir 26 (2010) 17558.
[39] G.R. Meseck, A. Käch, S. Seeger, J. Phys. Chem. C 118 (2014) 24967.
[40] Z. Chen, X. Wang, F. Giuliani, A. Atkinson, J. Power, Sources 273 (2015) 486.
[41] S. Thiele, R. Zengerle, C. Ziegler, Nano Res. 4 (2011) 849.
[42] J. Joos, M. Ender, T. Carraro, A. Weber, E. Ivers-Tiffée, Electrochim. Acta 82 (2012) 268.
[43] H. Liu, J.M. Foster, A. Gully, S. Krachkovskiy, M. Jiang, Y. Wu, X. Yang, B. Protas, G.R. Goward, G.A. Botton, J. Power, Sources 306 (2016) 300.
[44] K. Matsuzakia, N. Shikazonob, N. Kasagia, J. Power, Sources 196 (2011) 3073.
[45] J.R. Wilson, W. Kobsiriphat, R. Mendoza, H.-Y. Chen, J.M. Hiller, D.J. Miller, K. Thornton, P.W. Voorhees, S.B. Adler, Scott A. Barnett, Nat. Mater. 5 (2006) 541.
[46] C. Netzeband, T. Arlt, K. Wippermann, W. Lehnert, J. Power, Sources 327 (2016) 481.
[47] L. Iannarelli, A.M. Giovannozzi, F. Morelli, F. Viscotti, P. Bigini, V. Maurino, G. Spoto, G. Martra, E. Ortel, V.-D. Hodoroaba, A.M. Rossi, L. Diomedec, RSC Adv. 6 (2016) 70501.
[48] M. Schaffer, B. Schaffer, Q. Ramasse, Ultramicroscopy 114 (2012) 62.
[49] V.-D. Hodoroaba, D. Akcakayiran, D.O. Grigoriev, D.G. Shchukin, Analyst 139 (2014) 2004.
[50] F.J.W.-M. Leong, M. Brady, J.O'D. McGee, J. Clin. Pathol. 56 (2003) 619.
[51] B. Münch, P. Trtik, F. Marone, M. Stampanoni, Opt. Express 17 (2009) 8567.
[52] C.A. Schneider, W.S. Rasband, K.W. Eliceiri, Nat. Methods 9 (2012) 671.
[53] N. Otsu, IEEE Trans. Sys. Man. Cybern. 9 (1979) 62.
[54] J. Sauvola, M. Pietaksinen, Pattern Recogn. 33 (2000) 225.
[55] N. Phansalkar, S. More, A. Sabale, M. Joshi, International Conference on Communications and Signal Processing (ICCSP), (2010), p. 218.
[56] G.H. Ball, D.J. Hall, Stanford research institute, Menlo Park, CA, Technical Report AD, 699616 (1965).
[57] DIN 66138, Isothermal Measurement of the Sorption of Vapors at Solids, (2008).
[58] F. Babick, J. Mielke, W. Wohlleben, S. Weigel, V.-D. Hodoroaba, J. Nanopart. Res. 18 (2016) 158.
[59] V. Kestens, G. Roebben, J. Herrmann, Å. Jämting, V. Coleman, C. Minelli, C. Cliffford, P.-J. De Temmerman, J. Mast, L. Junjie, F. Babick, H. Cölfen, H. Emons, J. Nanopart. Res. 18 (2016) 171.
[60] H.G. Jones, K.P. Mingard, D.C. Cox, Ultramicroscopy 139 (2014) 20.
[61] J.Q. Gan, A.B. Yu, Z.Y. Zhou, Chem. Eng. Sci. 156 (2016) 64.
[62] D.J. Cumberland, R.J. Crawford, The packing of particles, in: J.C. Williams, T. Allen (Eds.), Handbook of Powder Technology, Elsevier, Amsterdam, 1987, pp. 85–118.
[63] J. Joos, T. Carraro, M. Ender, B. Rüger, A. Weber, E. Ivers-Tiffée, ECS Trans. 35 (2011) 2357.